

The CoSe₂ hollow cube/CoSe₂ nanosheet interface catalyst for efficient electrolysis of urea-assisted hydrogen production at industrial-grade currents

Borong Lu ^a, Zhuo Li ^a, Jinling Yin ^a, Kai Zhu ^a, Ke Ye ^{a,b,*}

^a Key Laboratory of Superlight Materials and Surface Technology of Ministry of Education, College of Materials Science and Chemical Engineering, Harbin Engineering University, Harbin 150001, China

^b Qingdao Institute of Bioenergy and Bioprocess Technology, Chinese Academy of Sciences, Qingdao 266101, China



ARTICLE INFO

Keywords:

Interface strategy
Avoid CSOR
Urea oxidation reaction
Urea-rich water purification

ABSTRACT

Cobalt-based catalysts are regarded as the most innovative catalyst in the urea oxidation reaction (UOR). Nevertheless, the activity limitation of Co-based catalysts by the unavoidable self-oxidation reaction of Co species (CSOR) during UOR is generally ignored. Therefore, the interface strategy was used to synthesize a CoSe₂ hollow cube (HC)/CoSe₂ nanosheet (NS) homogeneous interface catalyst to achieve bifunctional UOR and HER performance. In situ EIS, ex situ Raman spectroscopy, and ex situ XPS analysis verify the unique mechanism of the CoSe₂ HC/CoSe₂ NS interface in triggering UOR. Electrochemical activity tests demonstrated that CoSe₂ HC/CoSe₂ NS requires only 1.27 and 1.32 V of cell voltage to reach 10 mA cm⁻² in the overall urea electrolyzer (UOR || HER) and overall human urine electrolyzer (HUOR || HER) regimes, respectively. Moreover, under an industrial-grade current (500 mA cm⁻²), the cell voltage can be maintained at < 2 V for 110 h. Ultraviolet (UV) spectroscopy confirms the potential of CoSe₂ HC/CoSe₂ NS to degrade urea wastewater. Software simulations reveal the advantages of the unique interface strategy of CoSe₂ HC/CoSe₂ NS in the UOR process.

1. Introduction

Development of advanced electrocatalytic technology to convert urea-rich wastewater into clean energy to satisfy the concept of sustainable, efficient, and green energy [1–7]. Urea oxidation reaction (UOR) has gained attention as a crucial process for the electrolysis of urea-rich wastewater, and can simultaneously degrade urea and produce a green hydrogen resource. Notably, urea electrolysis-assisted hydrogen production theoretically saves up to 70% of electrical energy consumption at the anode (vs OER) compared to conventional hydrogen production from electrochemical water splitting [8,9]. This is because UOR possess a thermodynamic equilibrium potential of 0.37 V (versus the reversible hydrogen electrode (RHE)) that is much lower than that of the oxygen evolution reaction (OER) 1.23 V of conventional water splitting, and suitable for matching the kinetic rate of the cathodic hydrogen evolution reaction (HER), thus UOR has great potential to be a candidate for replacing the OER in the sustainable production of hydrogen [10–12]. Despite the obvious advantages of UOR, the

intrinsically slow kinetics inherent in the coupled six electron-proton transfer process of UOR and the complex adsorption/desorption intermediates generated in the reaction seriously affect the stability and activity of the electrocatalysts [13,14]. Therefore, the development of efficient, sustainable, and green electrocatalysts to accelerate electrolysis urea-assisted hydrogen production and realize large-scale industrial-scale applications are urgently needed.

Recently, cobalt-based catalysts are of interest due to their high activity, favorable electronic structure, and economic friendliness. Thus, researchers have proposed some groundbreaking strategies for cobalt-based materials to enhance electrocatalytic activity. Such as the introduction of heteroatoms [15–17], defect engineering [18,19], and atom dispersion [20,21] to optimize the electronic structure of catalysts and accelerate reaction kinetics. These strategies may change the inherent atomic structure and lattice order of the catalyst material, thereby improving the catalytic activity. Previous reports demonstrated that most cobalt-based materials possess a self-oxidation process in the reaction, and the generated CoOOH is considered to be the catalytically

* Corresponding author at: Key Laboratory of Superlight Materials and Surface Technology of Ministry of Education, College of Materials Science and Chemical Engineering, Harbin Engineering University, Harbin 150001, China.

E-mail address: yeke@hrbeu.edu.cn (K. Ye).

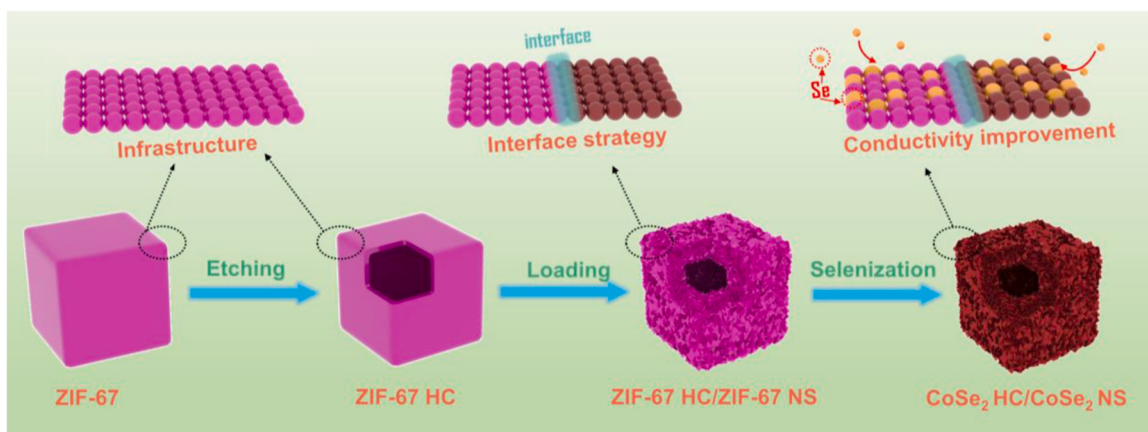


Fig. 1. Schematic of the synthesis of CoSe₂ HC/CoSe₂ NS interface catalyst.

active substance and the real active site in UOR [22]. However, the catalyst activity is limited to a large extent by the unavoidable self-oxidation reaction of Co species (CSOR). The self-oxidation process of the catalyst leads to the dissolution of the active metal sites at the expense of catalytic stability. Besides, it causes the UOR process to behind the Co oxidation reaction process, which requires excessive potential to drive the UOR, causing electrical energy consumption [23–25]. Interface chemical construction engineering has emerged as a novel powerful improvement strategy. This is due to the advantage that the catalyst combines individual components, regulating the redistribution of electrons around the active center and accelerating the reaction kinetics [26,27]. However, the interface catalyst has rarely been reported in UOR, and not mention interface catalysts suitable for maintaining stability at industrial-grade current density. Therefore, rationally constructing an interface catalyst applied in UOR to avoid the influence of the CSOR triggering mechanism and maintain normal operation and durability at industrial current densities is of great significance from both theoretical and practical perspectives.

Therefore, a novel CoSe₂ hollow cube (HC)/CoSe₂ nanosheet (NS) interface catalyst was constructed by template etching, solvothermal, and selenization processes in the context of interface chemistry strategy. Triggers UOR before CSOR and maintains operational stability at industrial-grade current densities. In situ EIS, ex situ Raman spectroscopy, and ex situ XPS analysis confirm that UOR initiation is prioritized before CSOR at the CoSe₂ HC/CoSe₂ NS interface. Meanwhile, the unique hollow structure provides a rapid release of gases during the reaction and avoids the retention of gases that may affect the catalytic activity. The CoSe₂ HC/CoSe₂ NS exhibited excellent UOR and HER activities with overpotentials of 50 mV and 44.5 mV at 10 mA cm⁻² current density, respectively. Notably, in the industrial-grade overall urea electrolyzer (HER||UOR), CoSe₂ HC/CoSe₂ NS holds cell voltage of 1.65 V at 500 mA cm⁻² for 110 h without significant degradation. Meanwhile, in the industrial-grade overall human urine electrolyzer (HER||HUOR), CoSe₂ HC/CoSe₂ NS still maintains a cell voltage of 1.85 V at the same current density for 110 h. The CoSe₂ HC/CoSe₂ NS demonstrates the potential for electrolytic treatment of urea wastewater. In addition, UV-visible spectrophotometry demonstrated that CoSe₂ HC/CoSe₂ NS possesses the capacity to electrochemically degrade urea. Software simulations reveal the advantages of unique interface strategies in the UOR process.

2. Experimental section

2.1. Synthesis of ZIF-67 cubes

The Co(NO₃)₂·6 H₂O (1.0 mmol) and cetyltrimethylammonium bromide (0.3 mmol) were placed together in a beaker of 30 mL

deionized water and stirred for 30 minutes at 25°C. Subsequently, rapidly inject 14 mL containing 0.9 mmol of 2-methylimidazole (C₄H₆N₂) and stir for 20 minutes. Finally, the product was washed three times with ethanol and vacuum dried at room temperature.

2.2. Synthesis of ZIF-67 hollow cubes

Disperse 60 mg of ZIF-67 cubes into 20 mL of ethanol, and pour 300 mL containing 1 mg/mL of tannic acid: ethanol: water (1:1:1), stir for 10 min, centrifuge to collect the product, wash with ethanol several times, and dry at 70 °C.

2.3. Synthesis of ZIF-67 hollow cubes /ZIF-67 nanosheet

Co(NO₃)₂·6 H₂O and C₄H₆N₂ were respectively added to 15 mL of methanol, and stirred for 15 minutes. The product was then centrifuged twice at 11,000 rpm and added to the methanol mixture of Co (NO₃)₂·6 H₂O and C₄H₆N₂. ZIF-67 hollow cubes was dispersed into the above solution and stirred for 15 min. The homogeneous suspension was then transferred to a 50 mL Teflon-lined stainless steel autoclave in which a piece of treated NF (1.0 cm × 4.0 cm) was placed and heated to 120 °C for 1 h. Finally, it was thoroughly rinsed with deionized water and ethanol and dried at 60 °C for 12 h.

2.4. Synthesis of CoSe₂ hollow cubes/CoSe₂ nanosheet

The synthesis of CoSe₂ hollow cubes (HC)/CoSe₂ nanosheet (NS) requires selenide in a tube furnace. The prepared ZIF-67 hollow cubes/ZIF-67 nanosheet (ZIF-67 HC/ZIF-67 NS) and 300 mg of Se powder were separately placed in a porcelain boat, followed by placing the porcelain boat with Se powder upstream of the tube furnace and ZIF-67 HC/ZIF-67 NS downstream. It was then calcinated at 350°C for 2 h at a ramp rate of 5°C min⁻¹ and cooled to room temperature.

3. Results and discussion

3.1. Synthesis and structural characterization

The CoSe₂ HC/CoSe₂ NS interface catalyst is synthesized by our proposed facile three-step strategy as shown in Fig. 1. The ZIF-67 cubes substrate was first synthesized at room temperature and subsequently etched into hollow cubes by tannic acid. Subsequently, the ZIF-67 hollow cubes (ZIF-67 HC) were again immersed into the ZIF-67 containing solution by solvothermal synthesis of ZIF-67 hollow cubes/ZIF-67 nanosheet (ZIF-67 HC/ZIF-67 NS), to construct the interface. Finally, the obtained ZIF-67 HC/ZIF-67 NS was subjected to selenization in an argon (Ar) atmosphere at 350°C to obtain CoSe₂ HC/CoSe₂ NS.

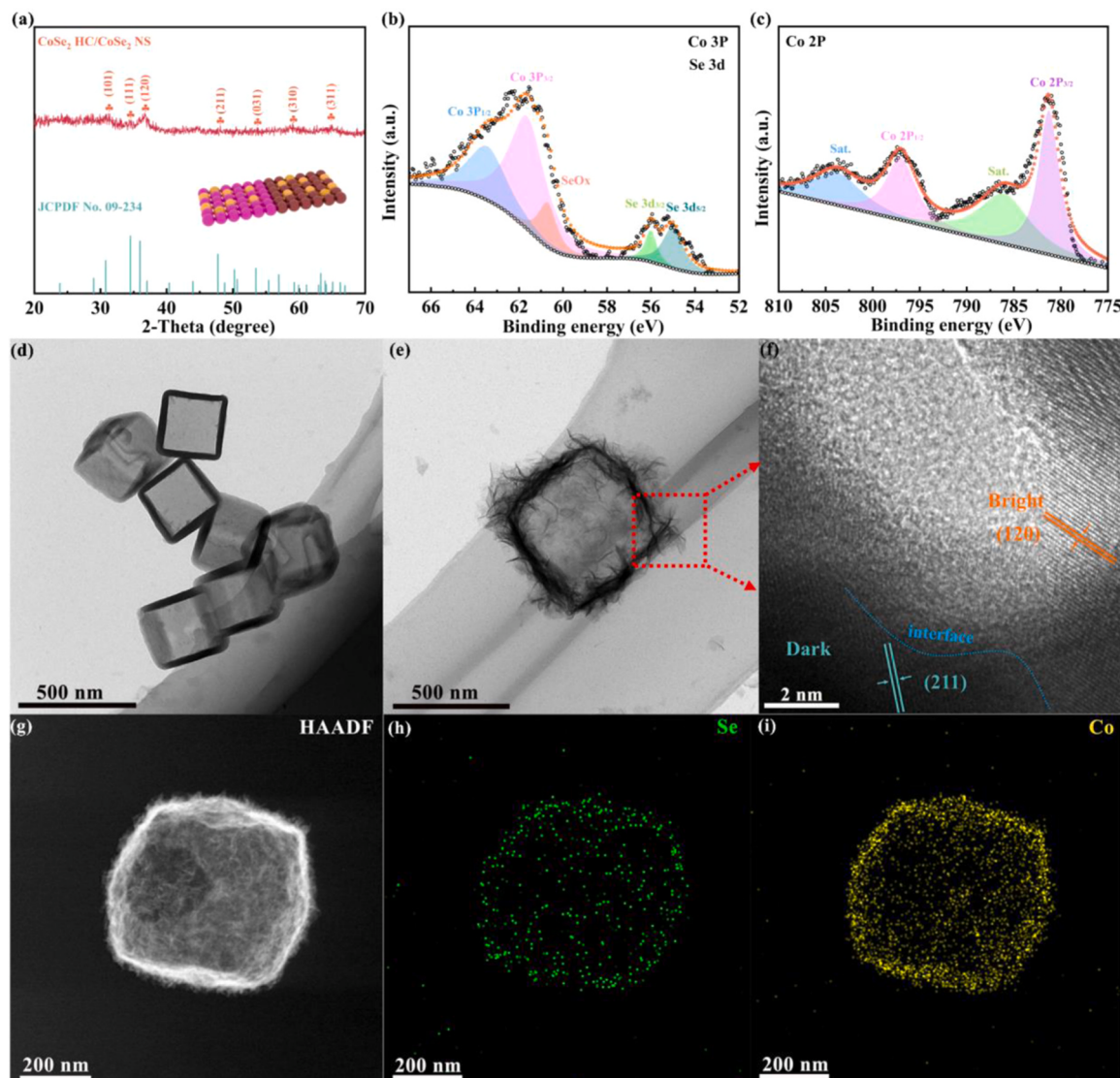


Fig. 2. (a) XRD patterns of CoSe_2 HC/ CoSe_2 NS; XPS of (b) Co 3p, Se 3d, and (c) Co 2p. TEM images of (d) CoSe_2 , (e) CoSe_2 HC/ CoSe_2 NS; (f) High-resolution TEM of CoSe_2 HC/ CoSe_2 NS; (g) HAADF. EDS elemental mapping images of the (h) Se, and (i) Co.

XRD measurements were performed to characterize the crystallinity of the CoSe_2 HC/ CoSe_2 NS interface catalyst. As depicted in Fig. 2a, the diffraction peaks observed at 30.78° , 34.51° , 35.97° , 47.72° , 53.48° , 59.26° , and 65.08° can be attributed to the fingerprint of CoSe_2 (JCPDF No. 09-234) (101), (111), (120), (211), (031), (310), and (311) lattice surfaces. Notably, no new diffraction peaks were observed in the formation of CoSe_2 HC/ CoSe_2 NS. However, the diffraction peaks were slightly shifted to a higher angle, suggesting the successful synthesis of CoSe_2 HC/ CoSe_2 NS and enhanced crystallinity. Electronic structure information of CoSe_2 HC/ CoSe_2 NS by X-ray photoelectron spectroscopy (XPS). The spectra of Se 3d are demonstrated in Fig. 2b. The Se 3d_{5/2} and Se 3d_{3/2} orbitals correspond to peaks at 54.7 and 55.8 eV, respectively. The presence of the peak at 60.6 eV may be related to the structure of the selenium–oxygen bonds [28]. Additionally, two strong peaks located at 61.6 and 63.5 eV are attributed

to Co 3p_{3/2} and Co 3p_{1/2}, respectively. The presence of Co3p indicates the formation of a Co–Se bond [29]. As shown in Fig. 2c, the peak at 781.2 eV is attributed to the Co 2p_{3/2} region. The other peak at 797.6 eV is attributed to the Co 2p_{1/2} region. Additionally, two satellite peaks were observed at 802.8 and 786.1 eV [30,31]. Besides, XPS examination spectra are provided in Fig. S1. Fig. 2d and Fig. S2 depict transmission electron microscopy (TEM) and scanning electron

microscopy (SEM) images of CoSe_2 hollow cube (HC), observed as hollow cubes. This was obtained by etching ZIF-67 cubes (Fig. S3). Compared with CoSe_2 HC, CoSe_2 HC/ CoSe_2 NS shows thin wrinkled nanosheets growing on its surface (Fig. 2e and Fig. S4). The high-resolution TEM (Fig. 2f) and corresponding selected area electron diffraction (SAED) patterns (Fig. S5) show well-defined lattice edges and diffraction rings. The lattice fringes of 0.201 and 0.263 nm are attributed to the (120) and (211) planes of CoSe_2 , respectively. Notably, there are distinct “dark” and “bright” regions between the two crystalline phases, with the “dark” regions attributed to the walls of the CoSe_2 hollow cubes and the bright regions attributed to the CoSe_2 thin nanosheets. In addition, there is a significant interface between the two different regions of the crystalline phase. This is consistent with the design of constructing the CoSe_2 HC/ CoSe_2 NS interface catalyst. The elements Co and Se are uniformly distributed on the CoSe_2 HC/ CoSe_2 NS as indicated by the energy-dispersive X-ray spectroscopy (EDS) mapping images (Fig. 2g–i).

3.2. UOR activity test

Evaluation of OER and UOR activity in 1 M KOH and 1 M KOH + 0.5 M urea electrolyte environments, respectively. As shown in Fig. 3a,

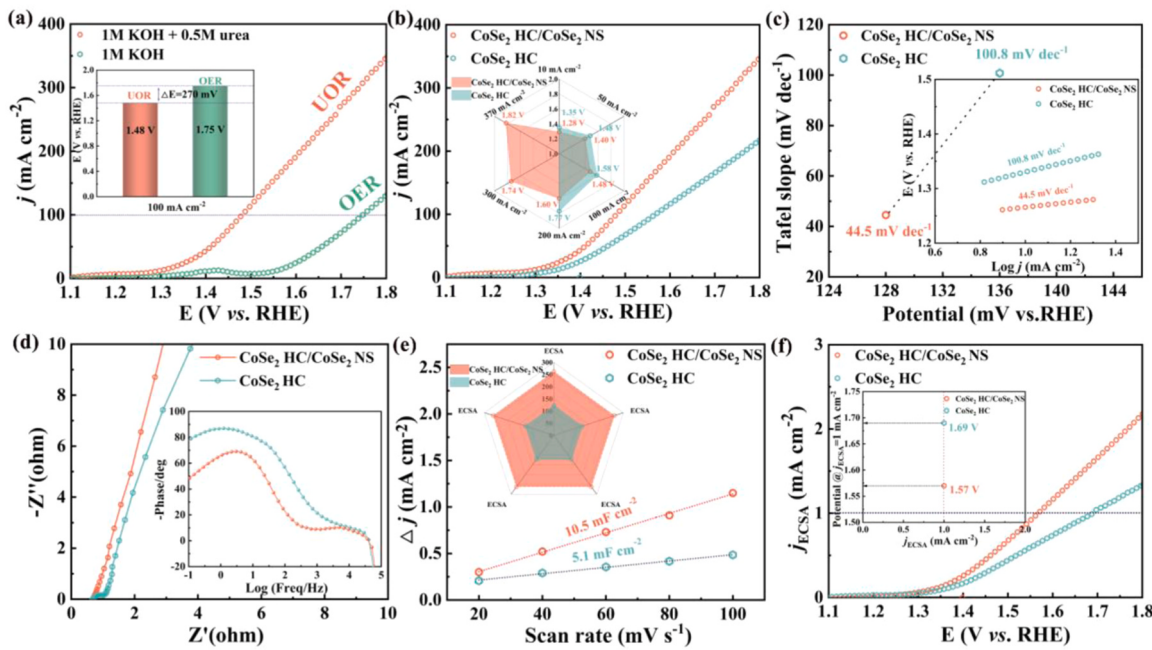


Fig. 3. (a) LSV curves for UOR and OER of CoSe₂ HC/CoSe₂ NS in 1 M KOH with and without 0.5 M urea environment, respectively; (b) UOR activity test for CoSe₂ HC/CoSe₂ NS and CoSe₂ HC; (c) Corresponding Tafel plots; (d) EIS test; (e) C_{dl} of the catalysts; (f) The ECSA–normalized LSV curves (j_{ECSA}).

CoSe₂ HC/CoSe₂ NS achieves 100 mA cm⁻² with a low potential of 1.48 V during UOR, saving 270 mV compared to OER. This suggests that UOR may become a potential substitute for OER-assisted hydrogen production. In addition, a significant oxidation peak at 1.43 V in the LSV curves during the OER process, which can be attributed to the Co²⁺→Co³⁺ transition due to the oxidation formation of Co species [32, 33]. Specifically, CoSe₂ HC/CoSe₂ NS exhibits a low potential of 1.28 V to reach a current density of 10 mA cm⁻² in an electrolyte containing 1 M KOH + 0.5 M urea, while CoSe₂ HC requires 1.35 V (Fig. 3b). Their potential gap further widens to 170 mV when the current density reaches 200 mA cm⁻². Especially in the range of 300–370 mA cm⁻², the potential of CoSe₂ HC is unattainable. This indicates that CoSe₂

HC/CoSe₂ NS has a significant advantage in catalyzing urea. Further evaluation of the UOR dynamics of CoSe₂ HC/CoSe₂ NS by LSV calculated Tafel slope. As shown in Fig. 3c, the Tafel slope of CoSe₂ HC/CoSe₂ NS (44.5 mV dec⁻¹) is much smaller than that of CoSe₂ HC (100.8 mV dec⁻¹), indicating that the unique interface of CoSe₂ HC/CoSe₂ NS promotes charge transfer accelerating UOR dynamics. The charge transfer resistance (R_{ct}) of CoSe₂ HC/CoSe₂ NS further indicates the essential role of the interface in expediting charge transfer kinetics (Fig. 3d and Fig. S6). Besides, the Bode plots demonstrate that CoSe₂ HC/CoSe₂ NS has the smallest phase angle, proving its excellent charge transfer performance in the UOR process. The electrochemically active surface area (ECSA) of the catalysts, an important parameter for

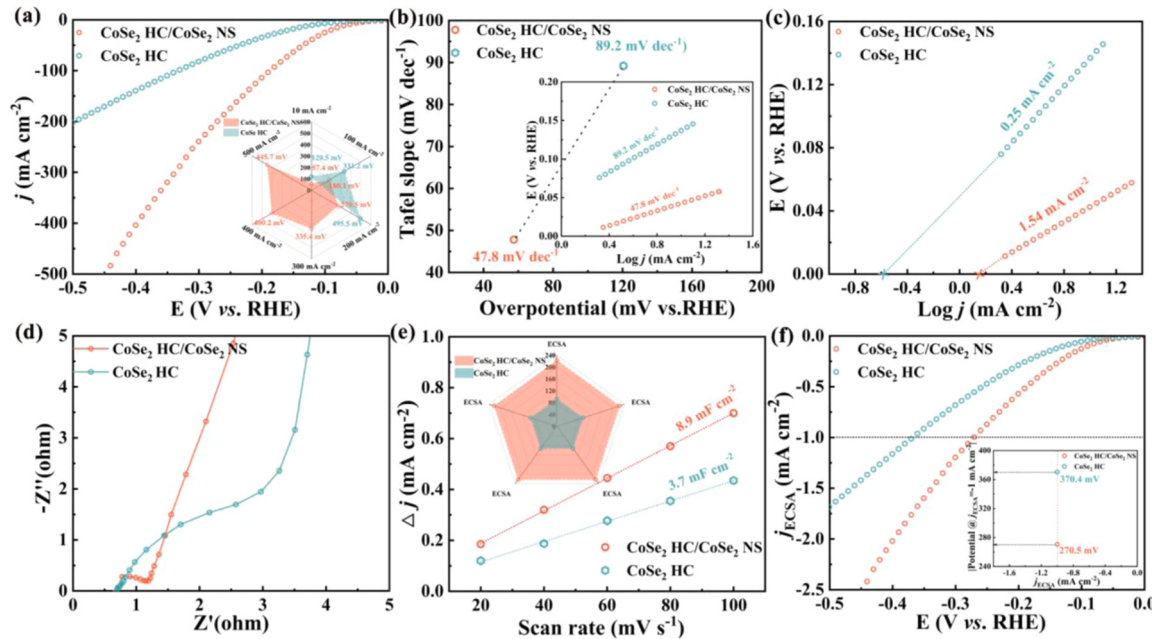


Fig. 4. (a) UOR activity test for CoSe₂ HC/CoSe₂ NS and CoSe₂ HC; (b) Tafel plots of the catalysts; (c) Exchange current density (j_0); (d) EIS test; (e) C_{dl} of the catalysts; (f) The ECSA–normalized LSV curves (j_{ECSA}).

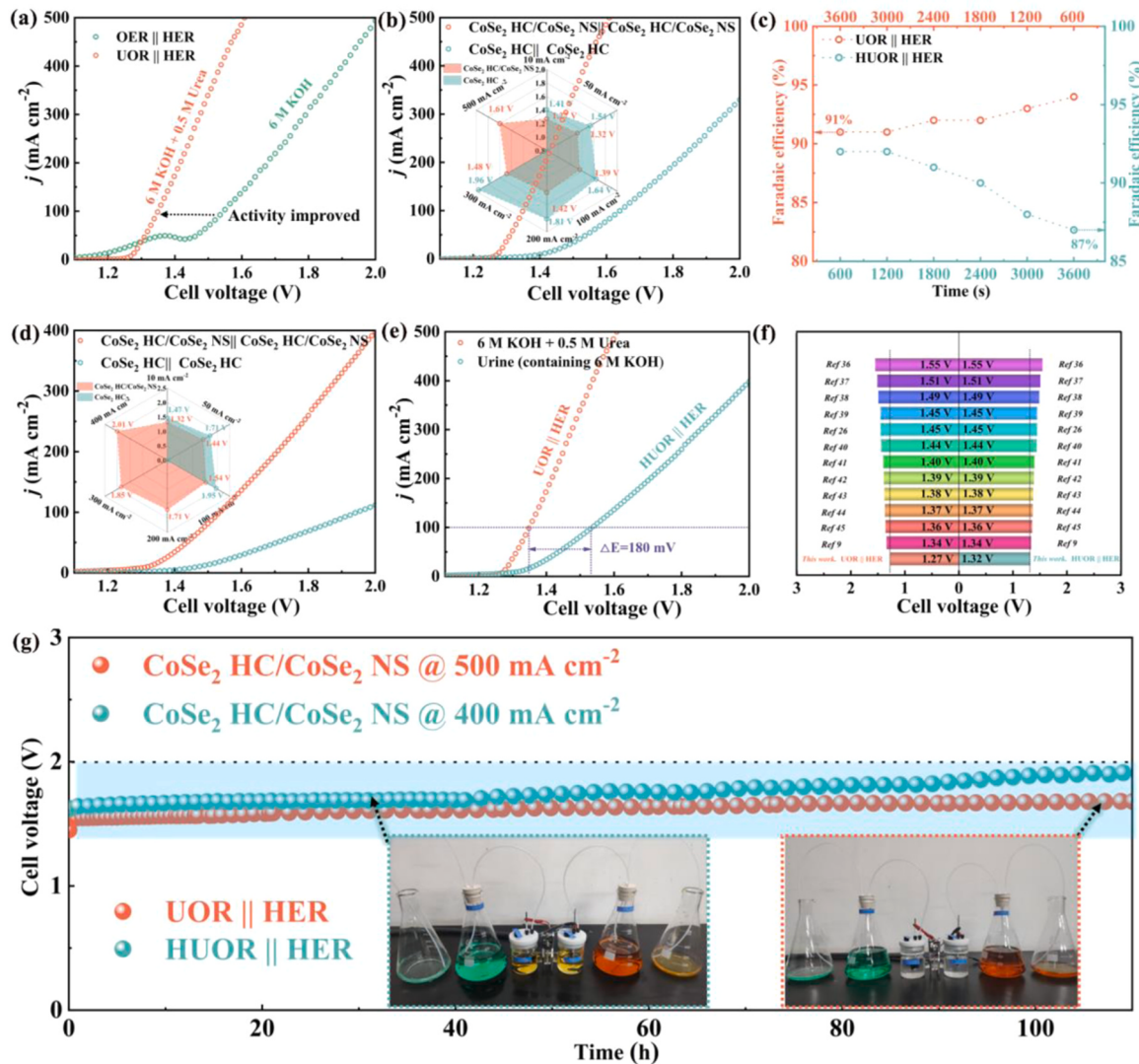


Fig. 5. (a) LSV curves for OER || HER and UOR || HER coupling systems of CoSe₂ HC/CoSe₂ NS in 6 M KOH with and without 0.5 M urea environment, respectively; (b) UOR || HER activity test for CoSe₂ HC/CoSe₂ NS and CoSe₂ HC; (c) Faradaic efficiency; (d) Activity test of catalysts in HUOR || HER coupling system; (e) Comparison of activity for UOR || HER and HUOR || HER systems; (f) Comparison of catalyst and reported performance; (g) Stability test of CoSe₂ HC/CoSe₂ NS in UOR || HER and HUOR || HER systems at industrial current density.

evaluating the electrocatalytic activity, was estimated by determining the double-layer capacitance (C_{dl}) from CV curves at different sweep speeds (Fig. 3e and Fig. S7). The C_{dl} value of CoSe₂ HC/CoSe₂ NS (10.5 mF cm⁻²) is higher than a single CoSe₂ HC (5.1 mF cm⁻²) and the active area is ~2.5 times larger than that of CoSe₂ HC, further indicating that the construction of the interface increases the catalyst active sites. As shown in Fig. 3f, The ECSA-normalized LSV curves (j_{ECSA}) further evaluate the UOR intrinsic activity of electrocatalysts, and CoSe₂ HC/CoSe₂ NS (1.57 V) requires only a smaller potential at 1 mA cm⁻² compared to CoSe₂ (1.69 V).

3.3. HER activity test

Similarly, electrochemical measurements were used to evaluate the HER activity of the catalysts in 1 M KOH. As illustrated in Fig. 4a, the overpotential of $\text{CoSe}_2\text{ HC}/\text{CoSe}_2\text{ NS}$ at a current density of 10 mA cm^{-2} is 57.4 mV, which is significantly smaller than $\text{CoSe}_2\text{ HC}$ (120.5 mV). Especially in the high current density environment of $300\text{--}500 \text{ mA cm}^{-2}$, only $\text{CoSe}_2\text{ HC}/\text{CoSe}_2\text{ NS}$ can continue to maintain HER activity. In addition, $\text{CoSe}_2\text{ HC}/\text{CoSe}_2\text{ NS}$ exhibited higher HER activity than commercial Pt/C electrodes at higher current densities.

(Fig. S8). The catalyst activity was further evaluated by the Tafel slope. The CoSe₂ HC/CoSe₂ NS exhibits a 47.8 mV dec⁻¹, which is superior to the 89.2 mV dec⁻¹ of CoSe₂ HC (Fig. 4b). In addition, their slopes are all between 40–120 mV dec⁻¹, indicating that the HER process follows the Volmer–Heyrovsky mechanism [34,35]. To further understand the reason for the enhanced CoSe₂ HC/CoSe₂ NS HER activity, we extrapolated the exchange current density (j_0) of the catalysts (Fig. 4c). Similarly, CoSe₂ HC/CoSe₂ NS has a j_0 value of 1.54 mA cm⁻², which is ~6.2 times that of CoSe₂ HC (0.25 mA cm⁻²). Tafel and j_0 reveal faster reaction kinetics for CoSe₂ HC/CoSe₂ NS. Further, the HER kinetics of the catalysts were evaluated by electrochemical impedance spectroscopy (EIS). The measured EIS Nyquist plots profile was fitted by the fitted charge transfer resistance (R_{ct}) value of CoSe₂ HC/CoSe₂ NS was 0.57 Ω (Fig. 4d), which is lower than that of CoSe₂ HC (3.24 Ω). CoSe₂ HC/CoSe₂ NS exhibits the fastest charge transfer rate, and these results about kinetics demonstrate that the construction of the interface of CoSe₂ HC/CoSe₂ NS can accelerate the HER kinetics. Similarly, the electrochemical surface area (ECSA) was evaluated by the double-layer capacitance (C_{dl}) derived from the CV curves (Fig. 4e and Fig. S9).

The C_{dl} value of CoSe₂ HC/CoSe₂ NS is 8.9 mF cm⁻², ~2.4 times larger than the C_{dl} value of CoSe₂ HC (3.7 mF cm⁻²). This suggests that

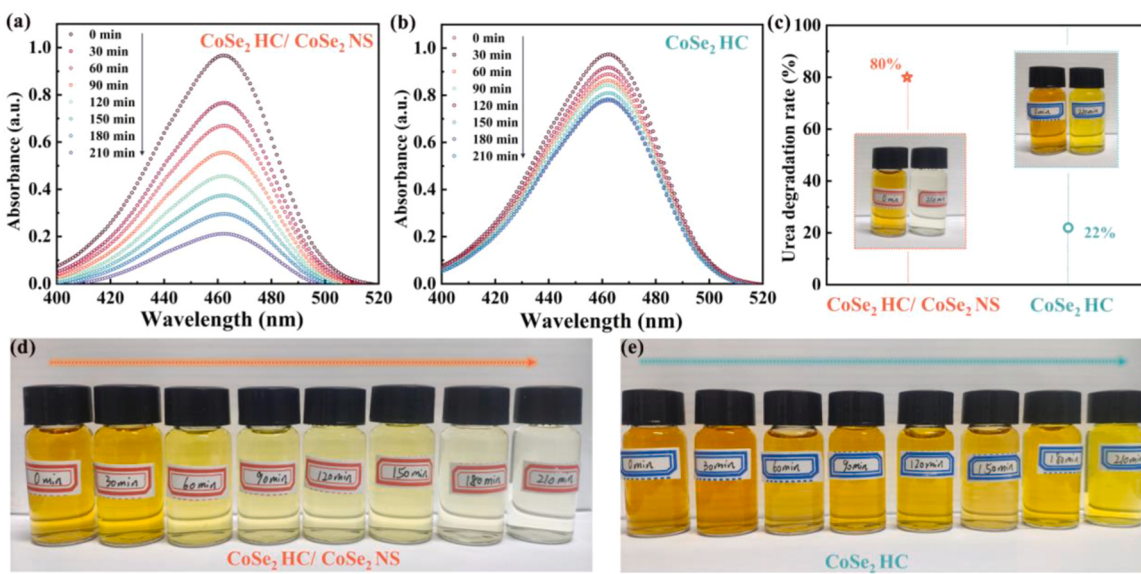


Fig. 6. UV spectrum of CoSe₂ HC/CoSe₂ NS (a) and CoSe₂ HC (b) during electrochemical degradation of urea (from 0 to 210 min at 30 min intervals); (c) Corresponding urea degradation rate; Color changes during urea degradation of CoSe₂ HC/CoSe₂ NS (d) and CoSe₂ HC (e).

the significant increase in the electrochemically active area of CoSe₂ HC/CoSe₂ NS should be due to the formation of interfaces exposing more catalytically active sites. The ECSA-normalized LSV (j_{ECSA}) exhibits that CoSe₂ HC/CoSe₂ NS has the smallest overpotential (270.5 mV) at 1 mA cm⁻² (Fig. 4f). Further evidence is that CoSe₂ HC/CoSe₂ NS has the best intrinsic activity.

3.4. Catalytic activity of the overall electrolyzer and purification performance of urea-rich wastewater

Overall urea electrolyzer (UOR || HER) and overall human urine electrolyzer (HUOR || HER) assembled with CoSe₂ HC/CoSe₂ NS as cathode and anode based on the excellent UOR and HER bifunctional electrocatalytic activity of CoSe₂ HC/CoSe₂ NS. Notably, the assembly of the HUOR || HER system permits a better evaluation of the real ability of the catalysts in the electrolytic treatment of urea-rich wastewater. In the context of industrial hydrogen production, to construct an energy-efficient and stable hydrogen production system, the performance of the CoSe₂ HC/CoSe₂ NS in overall urea electrolyzer was evaluated under industrial (6 M KOH + 0.5 M urea and 60 °C) and laboratory-grade (1 M KOH + 0.5 M urea and room temperature) conditions, respectively (Fig. S10). The overall urea electrolyzer of CoSe₂ HC/CoSe₂ NS achieves more satisfactory activity under industrial grade conditions, and the cell voltages of ~1.35 and ~1.61 V are required to provide current densities of 100 and 500 mA cm⁻², respectively, which are significantly better than the laboratory-grade performance. (Fig. S11).

As shown in Fig. 5a, CoSe₂ HC/CoSe₂ NS at 100 and 500 mA cm⁻² can be achieved in the UOR || HER system with cell voltages of only ~1.39 and ~1.61 V, respectively, and saving ~150 and ~390 mV compared to the OER || HER system. This proves that UOR is also an alternative to OER under industrial conditions. Compared to the UOR || HER system of CoSe₂ HC, CoSe₂ HC/CoSe₂ NS demonstrates superior energy efficiency (Fig. 5b), showing the interface advantage of CoSe₂ HC/CoSe₂ NS. The H₂ produced in the UOR || HER and HUOR || HER systems are quantified using the drainage method (Fig. S12), the Faradaic efficiency is 91%, and 87%, respectively (Fig. 5c and Fig. S13), indicating that CoSe₂ HC/CoSe₂ NS has a favorable ability to produce H₂ in both systems. As indicated in Fig. 5d, CoSe₂ HC/CoSe₂ NS exhibits considerable electrocatalytic activity in the HUOR || HER system compared to CoSe₂ HC individually, with current densities of 100 and 400 mA cm⁻² achievable with only 1.54 V and 2.01 V cell voltage,

respectively. For the comparison of the performance of CoSe₂ HC/CoSe₂ NS under UOR || HER and HUOR || HER systems, it is obvious that the UOR || HER system is more effective in reducing the cell voltage with increasing current density (Fig. 5e and Fig. S14). The slightly slower decrease in cell voltage in system HUOR || HER may be attributed to the fact that urine contains a certain amount of inorganic salts and uric acid, and it is impossible to avoid impurities affecting the catalytic performance of the UOR (Fig. S15) [36]. Even then, CoSe₂ HC/CoSe₂ NS outperforms the catalysts reported in many previous excellent works in both systems (Fig. 5f and Table S1) [9,26,37-46]. Notably, CoSe₂ HC/CoSe₂ NS can be maintained at < 2 V cell voltage for 110 h at industrial-grade current densities in both UOR || HER and HUOR || HER systems, respectively (Fig. 5g). This suggests that CoSe₂ HC/CoSe₂ NS maintains excellent stability even in the harsh environment of urine.

To further demonstrate the ability of CoSe₂ HC/CoSe₂ NS to purify urea-rich wastewater, we selected the diacetyl monooxime-antipyrine (national standard method) chemical technique to evaluate the efficiency of urea degradation. The absorption peak at 480 nm in the ultraviolet (UV) spectrum is the standard for certification of urea. As shown in Fig. 6a and b, CoSe₂ HC/CoSe₂ NS has a significant decrease in peak value in the UV test at 210 min, and CoSe₂ has decreased only slightly. In addition, the urea degradation rate of CoSe₂ HC/CoSe₂ NS was ~80.0% (Fig. 6c), which was higher than that of CoSe₂ (~22.0%). The color change from 0 to 210 min during urea degradation further demonstrates the potential of the catalyst for electrolysis of urea wastewater (Fig. 6d and e). This suggests that constructing an interface can effectively improve the urea degradation of CoSe₂ HC/CoSe₂ NS.

3.5. Catalytic mechanism analysis

To reveal the intrinsic mechanism of CoSe₂ HC/CoSe₂ NS in the UOR process. We performed in situ electrochemical impedance spectroscopy (EIS) analysis at different applied biases as an effective method to follow the interface dynamic, electron transfer, and dynamic evolution assessment. The significant oxidation peak can be observed in the LSV curve of OER shown in Fig. 7a, which corresponds to the transition from Co²⁺ to Co³⁺. This attributed to the formation of Co oxidation species [47,48]. The corresponding Bode plot shows a distinct phase peak in the 10⁰-10² Hz region (Fig. 7b), which can be attributed to the self-oxidation of the catalyst [49,50]. The distinct transition phase peak occurs in the 10⁻²-10⁻¹ Hz region at 1.60 V and exhibits decrease in the

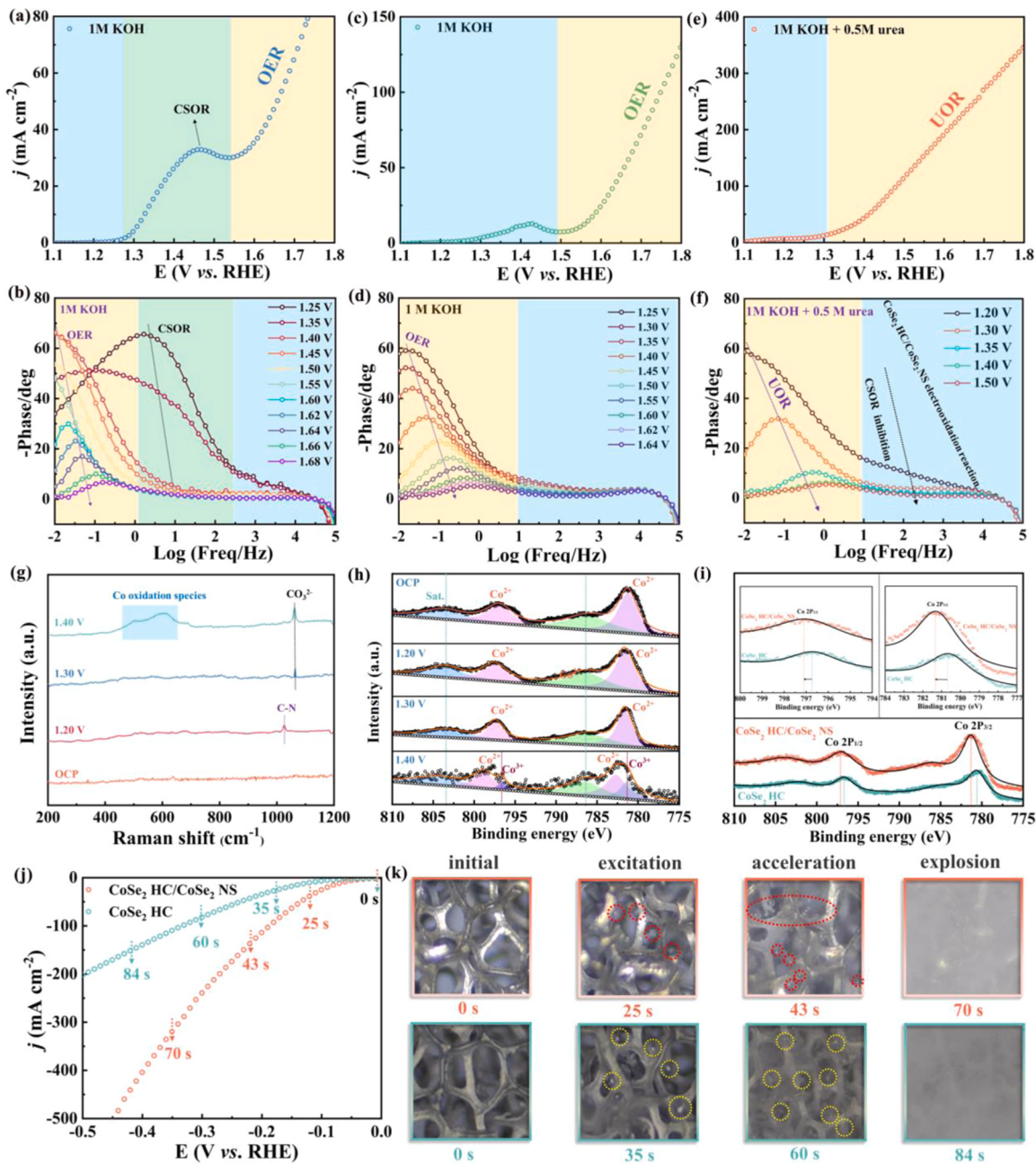


Fig. 7. Dynamic evaluation of catalysts during OER: LSV curves of CoSe₂ HC (a), and CoSe₂ HC/CoSe₂ NS (c); In situ EIS analysis of CoSe₂ HC, and CoSe₂ HC/CoSe₂ NS (d); Dynamic evaluation of UOR: (e) LSV curves of CoSe₂ HC/CoSe₂ NS; (f) In situ EIS analysis of CoSe₂ HC/CoSe₂ NS; (g) Ex situ Raman spectra of the CoSe₂ HC/CoSe₂ NS corresponding to the UOR Bode plots; (h) Ex situ XPS spectra; (i) Comparison of XPS spectra of CoSe₂ HC/CoSe₂ NS and CoSe₂ HC; (j) HER dynamic processes of CoSe₂ HC/CoSe₂ NS; (k) In situ optical microscopy of the reaction dynamic process.

phase peak and shift to higher frequency regions in the 1.60–1.70 V range. Therefore, as depicted in Fig. S16 and S17, the operating potential reaches 1.60 V, the two semicircles in the high-frequency region of Nyquist plot may be related to the oxidation of CoSe₂ HC, whereas the low-frequency region is related to the OER.

The insignificant oxidation peak in the OER of CoSe₂ HC/CoSe₂ NS, corresponding to the transition from Co²⁺ to Co³⁺ (Fig. 7c). In the corresponding Bode plot of Fig. 7d, there is no phase peak in the 10⁰–10² Hz region, which suggests that the constructed CoSe₂ HC/CoSe₂ NS interface can better avoid the self-oxidation reaction of the Co species. Correspondingly, the Nyquist plot exhibits two semicircles at 1.55 V (Fig. S18 and S19), the high-frequency region is attributed to the electrochemical oxidation reaction of the CoSe₂ HC/CoSe₂ NS, and exhibits good OER kinetics. After the addition of urea, no oxidation peaks are

observed in the LSV curves of UOR (Fig. 7e). The significant increase of current density in the oxidation potential range indicates that the active species promoting UOR is probably not CoOOH. The corresponding Bode plot exhibits a phase peak response in the 10⁻²–10⁻¹ Hz region (Fig. 7f). Specifically, a significant phase peak response is seen at 1.30 V, attributed to the UOR process, and no phase peaks were observed in the 10¹–10² Hz region. This further suggests that the UOR reaction occurs preferentially at the CoSe₂ HC/CoSe₂ NS interface rather than driven by active CoOOH generated by catalyst self-oxidation reaction. The corresponding Nyquist plot has two semicircles, demonstrating that CoSe₂ HC/CoSe₂ NS possess fast UOR dynamics (Fig. S20 and S21). Ex situ Raman spectrum demonstrated the dynamic reaction mechanism of CoSe₂ HC/CoSe₂ NS in the UOR process (Fig. 7g). The operating voltage reaches 1.20 V, a significant peak at ~1005 cm⁻¹ is attributed to the

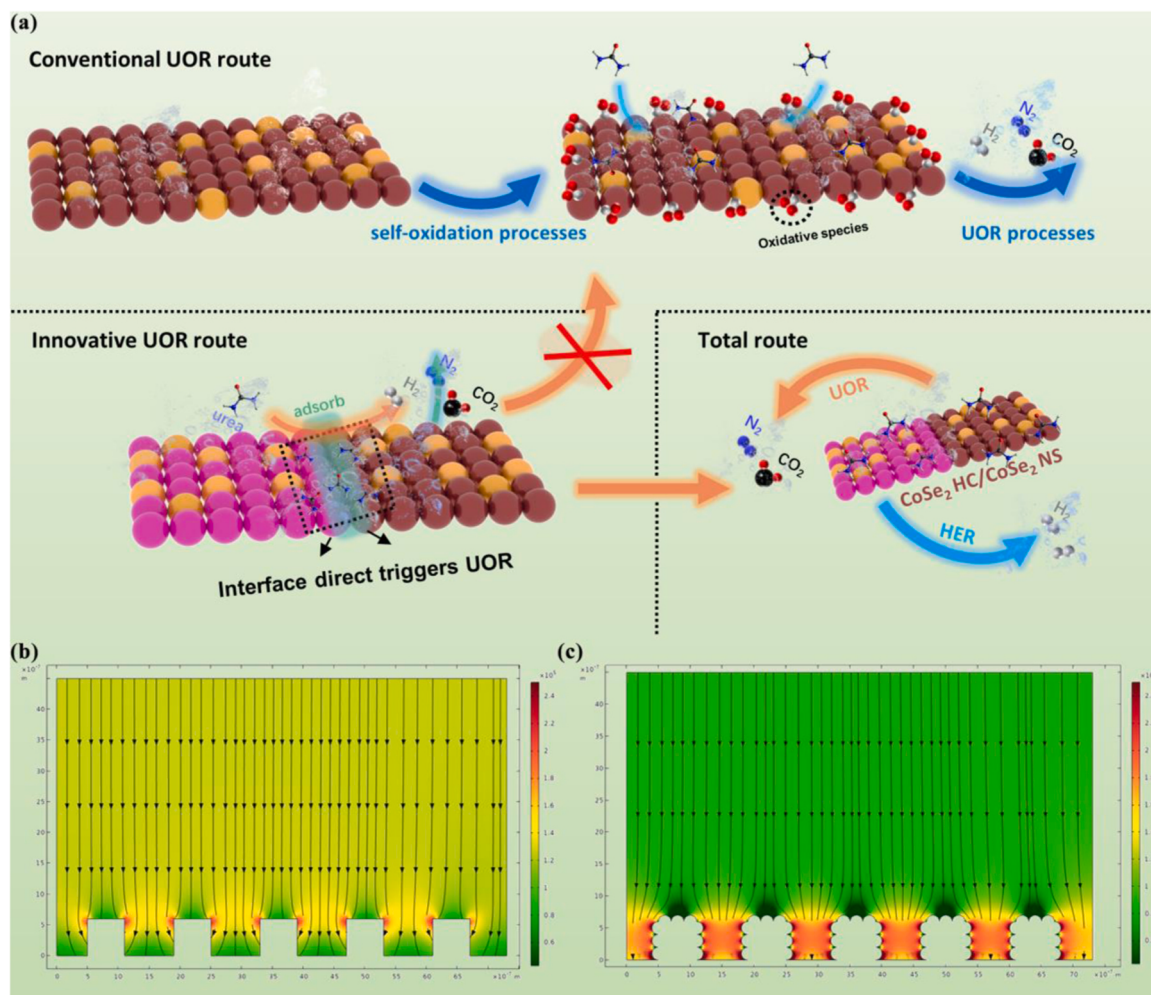


Fig. 8. (a) Schematic diagram of the UOR catalytic mechanism for CoSe₂ HC/CoSe₂ NS interface catalysts; Simulations of CoSe₂ HC/CoSe₂ NS (b) and CoSe₂ HC (c).

symmetric C–N stretch of urea [20], indicating rapid adsorption of urea molecules on the CoSe₂ HC/CoSe₂ NS surface. When the potential is increased to 1.30 V, a new peak appears at $\sim 1066\text{ cm}^{-1}$, corresponding to a symmetric extension of CO₃²⁻ from the UOR process producing CO₂ [23]. In addition, the two signal peaks at 1.40 V appearing at $\sim 480\text{ cm}^{-1}$ and $\sim 590\text{ cm}^{-1}$ are attribute to the vibration of Co–O [20,51]. This suggests the generation of Co oxidation species (CoOOH) at 1.40 V. Therefore, in combination with the LSV curve analysis of the UOR (Fig. 7e), indicates that the catalyst can be realized to drive the UOR at a low potential between 1.20 V–1.30 V. Notably, although the Co oxidation species formed at high potentials may serve as the active site for catalysis, CoSe₂ HC/CoSe₂ NS modulated by interface strategy can lead the overall catalytic reaction ahead of the formation of the oxidation species, providing a new UOR pathway.

Ex situ XPS further supports this opinion (Fig. 7h), with two distinct Co 2p peaks present near 797.4 and 781.5 eV when the voltage reaches 1.30 V, attributed to Co²⁺ species [52]. The new Co 2p peaks appearing at 781.2 and 796.5 eV during the voltage rise to 1.40 V were determined to be Co³⁺ species due to the formation of CoOOH during the UOR process [53,54]. Moreover, the presence of charge shift between the CoSe₂ HC/CoSe₂ NS interface was evaluated by XPS analysis in Fig. 7i. Obviously, the Co 2p peaks all move to higher binding energies compared to CoSe₂ HC, indicating the presence of charge transfer between the CoSe₂ HC/CoSe₂ NS interface [26]. The CoSe₂ HC/CoSe₂ NS interface catalyst based on the construction exhibited excellent bifunctional activity of HER and UOR (Fig. S22). The performance of the catalysts was further evaluated by the turnover frequency (TOF). TOF

can reflect the actual activity of each active site on the catalyst surface per unit time. As indicated in Fig. S23 and S24, the TOF value of CoSe₂ HC/CoSe₂ NS is the largest toward HER (0.75 s⁻¹) and UOR (1.14 s⁻¹), which indicates that CoSe₂ HC/CoSe₂ NS has the largest bifunctional electrocatalytic activity. Further, the HER process of the catalyst was observed by in-situ optical microscope. Through this in-situ method, the reaction degree of the catalyst and the release intensity of the corresponding gas can be observed in real-time. We divide the whole process of HER into initial → excitation → acceleration → explosion stages of CoSe₂ HC/CoSe₂ NS, and CoSe₂ HC (Movie S1 and S2). As shown in Fig. 7j and k, CoSe₂ HC/CoSe₂ NS excites the reaction for 25 s and small amounts of bubbles are observed to start producing on the electrode surface. When the reaction reaches 43 s, the whole reaction starts to accelerate and bubble production starts to increase. Finally, the reaction accelerates to 70 s with explosive gas release. In comparison to CoSe₂ HC, CoSe₂ HC/CoSe₂ NS demonstrated strong catalytic activity. This may be a result of the unique interface constructed. Thus, this unique interface chemistry strategy leads to a greater tendency for the UOR to occur before the self-oxidation reaction of the Co species, and this can greatly reduce the reaction barrier and thus the overpotential driving the UOR.

Supplementary material related to this article can be found online at doi:10.1016/j.apcatb.2024.123940.

Fig. 8a indicates the innovative UOR mechanism of action for the CoSe₂ HC/CoSe₂ NS interface catalyst, the urea molecule prefers to directly adsorb on the catalyst interface for the reaction, avoiding catalyst self-oxidation in conventional UOR reactions before driving the

reaction, which can significantly lower the reaction barrier. This unique reaction mechanism may be attributed to the charge density difference resulting from electron transfer generated between the CoSe₂ HC/CoSe₂ NS interface, which accelerates the driving of the UOR. Software simulations further reveal the advantages of the CoSe₂ HC/CoSe₂ NS interface for the UOR process. The exchange current density contour line shown in Fig. 8b and c, demonstrate that the CoSe₂ HC/CoSe₂ NS surface has a higher current density during the reaction process, as evidenced by the strong response of the current signals (red region) and denser current lines as compared to CoSe₂ HC. In addition, the voltage contour lines around CoSe₂ HC/CoSe₂ NS are denser and can trigger larger voltage changes (Fig. S25 and S26). Therefore, the interface properties of CoSe₂ HC/CoSe₂ NS optimize the potential distribution on the surface during the UOR process, which improves the exchange current density on the catalyst surface and promotes the overall catalytic process.

4. Conclusions

In summary, we propose a unique interface chemistry strategy to construct a unique CoSe₂ HC/CoSe₂ NS homogeneous structure to avoid the effect of CSOR on UOR. Characterization of the in situ electrochemical impedance spectroscopy, ex situ Raman spectroscopy, and ex situ XPS analysis verifies that CoSe₂ HC/CoSe₂ NS can trigger UOR before CSOR. An electrochemical in situ optical microscope further demonstrated the superior HER activity of CoSe₂ HC/CoSe₂ NS. In an industrial-scale overall urea electrolyzer (UOR || HER) environment, the CoSe₂ HC/CoSe₂ NS requires only 1.27 V cell voltage to achieve a current density of 10 mA cm⁻² and has significant long-term durability below 2 V cell voltage for 110 h at 500 mA cm⁻². Ultraviolet (UV) spectroscopy demonstrates the excellent ability of CoSe₂ HC/CoSe₂ NS to degrade urea. Meanwhile, the industrial-grade overall human urine electrolyzer (HUOR || HER) further demonstrated the potential of CoSe₂ HC/CoSe₂ NS to purify urea wastewater through electrolysis, and exhibit durable electrolytic ability even at 400 mA cm⁻² current density. Simulations reveal the advantages of the CoSe₂ HC/CoSe₂ NS interface in the UOR process. This work achieves optimized reaction pathways for UOR by designing CoSe₂ HC/CoSe₂ NS interface catalysts formed by assembling homogeneous structures and provides new insights for achieving electrochemical degradation of urea wastewater.

CRediT authorship contribution statement

Borong Lu: Writing – original draft, Methodology, Conceptualization. **Zhuo Li:** Software, Formal analysis. **Jinling Yin:** Validation, Data curation. **Kai Zhu:** Visualization, Validation. **Ke Ye:** Writing – review & editing, Methodology, Conceptualization.

Declaration of Competing Interest

The authors declare that they have no known financial interests/personal relationships that could influence the work reported in this paper.

Data availability

The authors do not have permission to share data.

Acknowledgements

This work was supported by QIBEBT International Cooperation Project (QIBEBT ICP202303), the Taishan Scholars Program and the Fundamental Research Funds for the Central Universities.

Appendix A. Supporting information

Supplementary data associated with this article can be found in the

online version at doi:10.1016/j.apcatb.2024.123940.

References

- [1] Y.G. Zhao, D.P.A. Saseendran, C. Huang, C.A. Triana, W.R. Marks, H. Chen, H. Zhao, G.R. Patzke, Oxygen evolution/reduction reaction catalysts: from in situ monitoring and reaction mechanisms to rational design, *Chem. Rev.* 123 (2023) 6257–6358.
- [2] Y.K. Chen, J.Y. Yu, J. Jia, F. Liu, Y.W. Zhang, G.W. Xiong, R.T. Zhang, R.Q. Yang, D.H. Sun, H. Liu, W.J. Zhou, Metallic Ni₃Mo₃N porous microrods with abundant catalytic sites as efficient electrocatalyst for large current density and superstability of hydrogen evolution reaction and water splitting, *Appl. Catal. B Environ.* 272 (2020) 118956.
- [3] J.Y. Chen, Y.K. Kang, W. Zhang, Z.H. Zhang, Y. Chen, Y. Yang, L.L. Duan, Y.F. Li, W. Li, Lattice-confined single-atom Fe₁S_x on mesoporous TiO₂ for boosting ambient electrocatalytic N₂ reduction reaction, *Angew. Chem. Int. Ed.* 61 (2022) e202203022.
- [4] K. Ye, Z.W. Zhou, J.Q. Shao, L. Lin, D.F. Gao, N. Ta, R. Si, G.X. Wang, X.H. Bao, In situ reconstruction of a hierarchical Sn-Cu/SnO_x core/shell catalyst for high-performance CO₂ electroreduction, *Angew. Chem. Int. Ed.* 59 (2020) 4814–4821.
- [5] H.S. Cao, P.Z. Qiao, Q.L. Zhong, R.J. Qi, Y.J. Dang, L. Wang, Z.A. Xu, W. Zhang, In situ reconstruction Ni-O octahedral active sites for promoting electrocatalytic oxygen evolution of nickel phosphate, *Small* 19 (2023) 2204864.
- [6] G.Y. Xing, M.M. Tong, P. Yu, L. Wang, G.Y. Zhang, C.G. Tian, H.G. Fu, Reconstruction of highly dense Cu-N₄ active sites in electrocatalytic oxygen reduction characterized by operando synchrotron radiation, *Angew. Chem. Int. Ed.* 61 (2022) e202211098.
- [7] K. Ye, T.F. Liu, Y.P. Song, Q. Wang, G.X. Wang, Tailoring the interactions of heterogeneous Ag₂S/Ag interface for efficient CO₂ electroreduction, *Appl. Catal. B: Environ.* 296 (2021) 120342.
- [8] L.Y. Zhang, Y.X. Wang, J. Cao, R. Zhang, F. Wang, H.M. Wu, Constructing rod-shaped Co₂C/MoN as efficient bifunctional electrocatalyst towards overall urea-water electrolysis, *Int. J. Hydrog. Energ.* 47 (2022) 34715–34726.
- [9] Z.X. Xu, S. Jin, M.H. Seo, X.L. Wang, Hierarchical Ni-Mo₂C/N-doped carbon Mott-Schottky array for water electrolysis, *Appl. Catal. B Environ.* 292 (2021) 120168.
- [10] J.Y. Zhang, J.Y. Liang, B.B. Mei, K. Lan, L.H. Zu, T.C. Zhao, Y.Z. Ma, Y. Chen, Z. R. Lv, Y. Yang, C.H. Yu, Z. Xu, B.Y. Xia, W. Li, Q.H. Yuan, D.Y. Zhao, Synthesis of Ni/NiO@MoO_{3-x} composite nanoarrays for high current density hydrogen evolution reaction, *Adv. Energy Mater.* 12 (2022) 2200001.
- [11] L.N. Sha, K. Ye, J.L. Yin, K. Zhu, K. Cheng, J. Yan, G.L. Wang, D.X. Cao, In situ grown 3D hierarchical MnCo₂O_{4.5}@Ni(OH)₂ nanosheet arrays on Ni foam for efficient electrocatalytic urea oxidation, *Chem. Eng. J.* 381 (2020) 122603.
- [12] J.P. Masnica, S. Sibt-e-Hassan, S. Potgieter-Vermak, Y.N. Regmi, L.A. King, L. Tosheva, ZIF-8-derived Fe-C catalysts: relationship between structure and catalytic activity toward the oxygen reduction reaction, *Green. Carbon* 1 (2023) 160–169.
- [13] T. Wang, H.M. Wu, C.Q. Feng, Y. Du, H. Mei, Ni, N-codoped NiMoO₄ grown on 3D nickel foam as bifunctional electrocatalysts for hydrogen production in urea-water electrolysis, *Electrochim. Acta* 391 (2021) 138931.
- [14] B.R. Lu, C.M. Lv, Y. Xie, L.X. Gao, J. Yan, K. Zhu, G.L. Wang, D.X. Cao, K. Ye, Exploring the synergistic effect of CoSeP/CoP interface catalyst for efficient urea electrolysis, *Small* 19 (2023) 2302923.
- [15] J.F. Kang, F. Yang, C. Sheng, H. Xu, J.Y. Wang, Y. Qing, Y.Q. Wu, X.H. Lu, CoP nanoparticle confined in P, N Co-doped porous carbon anchored on P-doped carbonized wood fibers with tailored electronic structure for efficient urea electro-oxidation, *Small* 18 (2022) 2200950.
- [16] Z.C. Wang, H.L. Liu, R.X. Ge, X. Ren, J. Ren, D.J. Yang, L.X. Zhang, X.P. Sun, Phosphorus-doped Co₃O₄ nanowire array: a highly efficient bifunctional electrocatalyst for overall water splitting, *ACS Catal.* 8 (2018) 2236–2241.
- [17] Q. Li, X.R. Li, J.W. Gu, Y.L. Li, Z.Q. Tian, H. Pang, Porous rod-like Ni₂P/Ni assemblies for enhanced urea electrooxidation, *Nano Res.* 14 (2021) 1405–1412.
- [18] J.W. Liang, S.B. Li, F.B. Li, L. Zhang, Y.F. Jiang, H.Y. Ma, K. Cheng, L. Qing, Defect engineering induces Mo-regulated Co₉Se₈/FeNiSe heterostructures with selenium vacancy for enhanced electrocatalytic overall water splitting in alkaline, *J. Colloid Interf. Sci.* 655 (2024) 296–306.
- [19] A. Kumar, X.H. Liu, J. Lee, B. Debnath, A.R. Jadhav, X.D. Shao, V.Q. Bui, Y. Hwang, Y. Liu, M.G. Kim, H. Lee, Discovering ultrahigh loading of single-metal-atoms via surface tensile-strain for unprecedented urea electrolysis, *Energy Environ. Sci.* 14 (2021) 6494–6505.
- [20] X.B. Zheng, J.R. Yang, P. Li, Z.L. Jiang, P. Zhu, Q.S. Wang, J.B. Wu, E. Zhang, W. P. Sun, S.X. Dou, D.S. Wang, Y.D. Li, Dual-atom support boosts nickel-catalyzed urea electrooxidation, *Angew. Chem. Int. Ed.* 62 (2023) e202217449.
- [21] J.C. Zhang, H.B. Yang, J.J. Gao, S.B. Xi, W.Z. Cai, J.M. Zhang, P. Cui, B. Liu, Design of hierarchical, three-dimensional free-standing single-atom electrode for H₂O₂ production in acidic media, *Carbon Energy* 2 (2020) 276–282.
- [22] Y.X. Hao, S.F. Hung, W.J. Zeng, Y. Wang, C.C. Zhang, C.H. Kuo, L.Q. Wang, S. Zhao, Y. Zhang, H.Y. Chen, S.J. Peng, Switching the oxygen evolution mechanism on atomically dispersed Ru for enhanced acidic reaction kinetics, *J. Am. Chem. Soc.* 145 (2023) 23659–23669.
- [23] M.Y. Liu, W.H. Zou, S.L. Qiu, N. Su, J. Cong, L.X. Hou, Active site tailoring of Ni-based coordination polymers for high-efficiency dual-functional HER and UOR catalysis, *Adv. Funct. Mater.* 34 (2024) 2310155.
- [24] Y.Q. Lei, T.T. Xu, S.H. Ye, L.R. Zheng, P. Liao, W. Xiong, J. Hu, Y.J. Wang, J. P. Wang, X.Z. Ren, C.X. He, Q.L. Zhang, J.H. Liu, X.L. Sun, Engineering defect-rich

- Fe-doped NiO coupled Ni cluster nanotube arrays with excellent oxygen evolution activity, *Appl. Catal. B Environ.* 285 (2021) 119809.
- [25] B. Zhang, J.W. Shan, W.L. Wang, P. Tsakaros, Y.Y. Li, Oxygen vacancy and core-shell heterojunction engineering of anemone-like CoP@CoOOH bifunctional electrocatalyst for efficient overall water splitting, *Small* 18 (2022) 2106012.
- [26] C.C. Li, Y.W. Liu, Z.W. Zhuo, H.X. Ju, D. Li, Y.P. Guo, X.J. Wu, H.Q. Li, T.Y. Zhai, Local charge distribution engineered by Schottky heterojunctions toward urea electrolysis, *Adv. Energy Mater.* 8 (2018) 1801775.
- [27] T.Z. Wang, L.C. Miao, S.Y. Zheng, H.Y. Qin, X.J. Cao, L. Yang, L.F. Jiao, Interfacial engineering of Ni₂N/Mo₂N heterojunctions for urea-assisted hydrogen evolution reaction, *ACS Catal.* 13 (2023) 4091–4100.
- [28] Y. Wang, X.Y. Sun, Y. Liu, S.Q. Zhang, F. Liu, Y. Li, Y.M. Xue, C.C. Tang, J. Zhang, Al-doping-induced electronic structure modulation of CoSe₂ for efficient hydrogen evolution reaction, *Fuel* 357 (2024) 129825.
- [29] Y.H. Zuo, D. Zhong, C. Huang, X.T. Ding, K. Qu, X.S. Wang, Y.H. Xu, CoSe₂ nanoparticles with multienzymatic activities for antibacterial applications, *ACS Appl. Nano Mater.* 6 (2023) 3357–3366.
- [30] Q. Hu, B. Zhu, G.M. Li, X.F. Liu, H.P. Yang, C.D. Sewell, Q.L. Zhang, J.H. Liu, C. X. He, Z.Q. Lin, Interconnected phosphorus-doped Co₃O₄-nanoparticles nanotube with three-dimensional accessible surface enables high-performance electrochemical oxidation, *Nano Energy* 66 (2019) 104194.
- [31] X. Zhang, F. Meng, S. Mao, Q. Ding, M.J. Shearer, M.S. Faber, J. Chen, R.J. Hamers, S. Jin, Amorphous Mo_xCl_y electrocatalyst supported by vertical graphene for efficient electrochemical and photoelectrochemical hydrogen generation, *Energy Environ. Sci.* 8 (2015) 862–868.
- [32] Z.L. Wang, W.J. Liu, Y.M. Hu, M.L. Guan, L. Xu, H.P. Li, J. Bao, H.M. Li, Cr-doped CoFe layered double hydroxides: highly efficient and robust bifunctional electrocatalyst for the oxidation of water and urea, *Appl. Catal. B: Environ.* 272 (2020) 118959.
- [33] N. Senthilkumar, G.G. Kumar, A. Manthiram, 3D hierarchical core-shell nanostructured arrays on carbon fibers as catalysts for direct urea fuel cells, *Adv. Energy Mater.* 8 (2018) 1702207.
- [34] H.M. Wu, C.Q. Feng, L. Zhang, J.J. Zhang, D.P. Wilkinson, Non-noble metal electrocatalysts for the hydrogen evolution reaction in water electrolysis, *Electrochim. Energy R.* 4 (2021) 473–507.
- [35] T. Wang, H.M. Wu, C.Q. Feng, L. Zhang, J.J. Zhang, MoP@NiCo-LDH on nickel foam as bifunctional electrocatalyst for high efficiency water and urea-water electrolysis, *J. Mater. Chem. A* 8 (2020) 18106–18116.
- [36] D.D. Li, F. Xu, X. Tang, S. Dai, T.C. Pu, X.L. Liu, P.F. Tian, F.Z. Xuan, Z. Xu, I. E. Wachs, M.H. Zhu, Induced activation of the commercial Cu/ZnO/Al₂O₃ catalyst for the steam reforming of methanol, *Nat. Catal.* 5 (2022) 99–108.
- [37] X.F. Lu, S.L. Zhang, W.L. Sim, S.Y. Gao, X.W. Lou, Phosphorized CoNi₂S₄ yolk-shell spheres for highly efficient hydrogen production via water and urea electrolysis, *Angew. Chem., Int. Ed.* 60 (2021) 22885–22891.
- [38] C. Wang, H.L. Lu, Z.Y. Mao, C.L. Yan, G.Z. Shen, X.F. Wang, Bimetal Schottky heterojunction boosting energy-saving hydrogen production from alkaline water via urea electrocatalysis, *Adv. Funct. Mater.* 30 (2020) 2000556.
- [39] K.X. Li, B.B. Xie, D.M. Feng, Y. Tong, Ni₂Se₃–CuSe_x heterostructure as a highly efficient bifunctional electrocatalyst for urea-assisted hydrogen generation, *ChemSusChem* 15 (2022) e202201656.
- [40] H.C. Sun, W. Zhang, J.G. Li, Z.S. Li, X. Ao, K.H. Xue, K.K. Ostrikov, J. Tang, C. D. Wang, Rh-engineered ultrathin NiFe-LDH nanosheets enable highly-efficient overall water splitting and urea electrolysis, *Appl. Catal. B: Environ.* 284 (2021) 119740.
- [41] X.C. Xu, H.J. Liao, L. Huang, S.J. Chen, R. Wang, S. Wu, Y.X. Wu, Z.P. Sun, H. T. Huang, Surface reconstruction and directed electron transport in NiSe₂/MoSe₂ Mott-Schottky heterojunction catalysts promote urea-assisted water splitting, *Appl. Catal. B: Environ.* 341 (2024) 123312.
- [42] T. Doana, D.C. Nguyen, K. Kang, A. Ponnusamy, H.I. Eyad, N.Y. Dzadad, C. S. Kim, C.H. Park, Advanced Mott-Schottky heterojunction of semi-conductive MoS₂ nanoparticles/metallic Co₃S₄ nanotubes as an efficient multifunctional catalyst for urea-water electrolysis, *Appl. Catal. B: Environ.* 342 (2024) 123295.
- [43] Z. Liu, C.Z. Zhang, H. Liu, L.G. Feng, Efficient synergism of NiSe₂ nanoparticle/NiO nanosheet for energy-relevant water and urea electrocatalysis, *Appl. Catal. B: Environ.* 276 (2020) 119165.
- [44] Z.Y. Yu, C.C. Lang, M.R. Gao, Y. Chen, Q.Q. Fu, Y. Duan, S.H. Yu, Ni-Mo–O nanorod-derived composite catalysts for efficient alkaline water-to-hydrogen conversion via urea electrolysis, *Energy Environ. Sci.* 11 (2018) 1890.
- [45] X.F. Xu, H. Ullah, M. Humayun, L.F. Li, X. Zhang, M. Bououdina, D.P. Debecker, K. F. Huo, D.L. Wang, C.D. Wang, Fluorinated Ni-O-C heterogeneous catalyst for efficient urea-assisted hydrogen production, *Adv. Funct. Mater.* 33 (2023) 2303986.
- [46] H. Jiang, M.Z. Sun, S.L. Wu, B.L. Huang, C.S. Lee, W.J. Zhang, Oxygen-incorporated NiMoP nanotube arrays as efficient bifunctional electrocatalysts for urea-assisted energy-saving hydrogen production in alkaline electrolyte, *Adv. Funct. Mater.* 31 (2021) 2104951.
- [47] A.S. Mary, C. Murugan, P. Murugan, A. Pandikumar, Unravelling the superior photoelectrochemical water oxidation performance of the Al-incorporated CoOOH cocatalyst-loaded BiVO₄ photoanode, *ACS Sustain. Chem. Eng.* 11 (2023) 13656–13667.
- [48] R. Ge, Y. Wang, Z. Li, M. Xu, S.M. Xu, H. Zhou, K. Ji, F. Chen, J. Zhou, H. Duan, Selective electrooxidation of biomass-derived alcohols to aldehydes in a neutral medium: promoted water dissociation over a nickel-oxide-supported ruthenium single-atom catalyst, *Angew. Chem. Int. Ed.* 61 (2022) e202200211.
- [49] Y. Qi, Y. Zhang, L. Yang, Y. Zhao, Y. Zhu, H. Jiang, C. Li, Insights into the activity of nickel boride/nickel heterostructures for efficient methanol electrooxidation, *Nat. Commun.* 13 (2022) 4602.
- [50] L. Wang, Y. Zhu, Y. Wen, S. Li, C. Cui, F. Ni, Y. Liu, H. Lin, Y. Li, H. Peng, B. Zhang, Regulating the local charge distribution of Ni active sites for the urea oxidation reaction, *Angew. Chem. Int. Ed.* 60 (2021) 10577–10582.
- [51] X. Zheng, Y. Chen, X. Zheng, G. Zhao, K. Rui, P. Li, X. Xu, Z. Cheng, S.X. Dou, W. Sun, Electronic structure engineering of LiCoO₂ toward enhanced oxygen electrocatalysis, *Adv. Energy Mater.* 9 (2019) 1803482.
- [52] Y. Liu, Z.L. Chen, H.X. Jia, H.B. Xu, M. Liu, R.B. Wu, Iron-doping-induced phase transformation in dual-carbon-confined cobalt diselenide enabling superior lithium storage, *ACS Nano* 13 (2019) 6113–6124.
- [53] J.N. Du, S.J. You, X.R. Li, B. Tang, B.J. Jiang, Y. Yu, Z. Cai, N.Q. Ren, J.L. Zou, In situ crystallization of active NiOOH/CoOOH heterostructures with hydroxide ion adsorption sites on velutines-like CoSe/NiSe nanorods as catalysts for oxygen evolution and cocatalysts for methanol oxidation, *ACS Appl. Mater. Inter.* 12 (2020) 686–697.
- [54] N. Yao, G.W. Wang, H.N. Jia, J.L. Yin, H.J. Cong, S.L. Chen, W. Luo, Intermolecular energy gap-induced formation of high-valent cobalt species in CoOOH surface layer on cobalt sulfides for efficient water oxidation, *Angew. Chem. Int. Ed.* 134 (2022) e202117178.